Astron. Astrophys. 350, 1018–1034 (1999)

ASTRONOMY AND ASTROPHYSICS

Two-dimensional simulation of solar granulation: description of technique and comparison with observations

A.S. Gadun[1], **S.K. Solanki**[2,3], **and A. Johannesson**[4]

[1] Main Astronomical Observatory of Ukrainian NAS, Goloseevo, 252650 Kiev-22, Ukraine
[2] Institute of Astronomy, ETH, 8092 Zürich, Switzerland
[3] Max-Planck-Institute of Aeronomy, Max-Planck-Strasse 2, 37191 Katlenburg-Lindau, Germany
[4] Big Bear Solar Observatory, 264-33 Caltech, Pasadena CA 91125, USA

Received 22 September 1997 / Accepted 22 July 1999

Abstract. The physical properties of the solar granulation are analyzed on the basis of 2-D fully compressible, radiation-hydrodynamic simulations and the synthetic spectra they produce. The basic physical and numerical treatment of the problem as well as tests of this treatment are described. The simulations are compared with spatially averaged spectral observations made near disk centre and high resolution spectra recorded near the solar limb. The present simulations reproduce a significant number of observed features, both at the centre of the solar disc and near the solar limb. Reproduced observables include the magnitude of continuum and line-core intensity fluctuations, line bisectors and correlations between different line parameters. Spatially averaged line shifts near disc centre, however, are not so well reproduced, as are individual correlations between line parameters near the solar limb. Possible causes of these discrepancies are discussed.

The present models predict the existence of two photospheric layers at which the temperature fluctuations change sign. We point out a diagnostic of the hitherto undetected upper sign reversal based on high spatial resolution spectral observations of a sample of lines formed over a wide range of heights in the photosphere.

Key words: hydrodynamics – line: formation – Sun: granulation – Sun: photosphere

1. Introduction

Hydrodynamic simulations of solar granular convection have reached a high level of maturity (e.g., Spruit et al. 1990, Stein & Nordlund 1998) and have passed a number of stringent observational tests (Dravins et al. 1981, 1986, Nordlund 1984b, Wöhl & Nordlund 1985, Lites et al. 1989, Steffen 1989, 1991, Steffen & Freytag 1991, Nordlund & Stein 1996, Gadun et al. 1997, Stein & Nordlund 1998).

The most successful granulation simulations have been those that explicitly take its three-dimensional (3-D) nature into account. They explain many aspects of solar granulation (see, e.g., Nordlund 1984a,b, Lites et al. 1989, Spruit et al. 1990, Stein & Nordlund 1998). 3-D models do have the disadvantage, however, that they are computationally expensive. This limits their applicability to the simulation of usually only a few convective cells of a given type (e.g., granulation). Statistical investigation of the properties of many granules, or simultaneous simulation of widely different scales of convection (e.g., granulation, mesogranulation and supergranulation) not only requires a fine grid covering a large computational domain, but also a long duration to cover the relevant turnover times, are easiest in 2-D. Such calculations will be the subject of future papers. This initial paper describes and tests the 2-D approach.

The strong claim on computational resources made by 3-D simulations also implies that simplifications need to be made in the description of some of the physical processes, principally the radiative transfer. Restricting ourselves to 2-D allows us to consider radiative energy transfer in greater detail and consequently at a greater level of realism than in 3-D. To test the influence of the description of the radiative transfer on the simulations is another aim of the present paper.

Our 2-D models need to reproduce a wide variety of observations if they are to form the basis of a better understanding of the physical processes responsible for solar convection

Some such tests have indeed been carried out in previous studies. Thus the distribution of sizes and lifetimes of 2-D simulated granules appear to be consistent with the observations (Gadun & Vorob'yov 1995, 1996). Temporal power spectra studied by Gadun & Pikalov (1996) possess two oscillation peaks ($T \sim$ 330–370 s and $T \sim$ 180–220 s), in qualitative agreement with observations and in excellent agreement with Fig. 2 of Stein et al. (1989). The power of the 3^m oscillations produced by the 2-D simulations grows with height in the atmosphere, leading to a tentative identification with chromospheric oscillations (e.g., Leibacher & Stein 1981). Gadun & Pikalov (1996) also qualitatively confirmed the relation between power spectra of temperature inhomogeneities and of kinetic energy fluctuations near the solar surface (Espagnet et al. 1993, but see Nordlund et al. 1997). Finally, the correlations between spatial variations of parameters of photospheric spectral lines have been

Send offprint requests to: S.K. Solanki (solanki@astro.phys.ethz.ch)

compared by Gadun et al. (1997) with the corresponding disc centre observations of Hanslmeier et al. (1990, 1991, 1994).

In the present paper we also compare the results of the simulations with a variety of observations, including bisectors and shifts of spatially averaged line profiles at disc centre (cf. Gadun 1995, 1996, 1998) as well as parameters of high-resolution observations near the limb.

Almost all previous comparisons between solar granulation simulations and observations have been restricted to the centre of the solar disc. Exceptions are the papers by Solanki et al. (1996), who searched for the signature of shocks near the limb guided by the predictions of numerical simulations, Nordlund (1984b) and Gadun (1986), who modeled the limb effect,[1] and investigations by Dravins & Nordlund (1990a, b) and Atroshchenko & Gadun (1994), who calculated profiles at different limb distances in order to reproduce observed stellar flux profiles. We explore here whether observations near the solar limb are able to provide more stringent constraints on granule simulations than observations near disc centre.

Some preliminary results of this investigation were published by Gadun et al. (1999b).

2. Two-dimensional radiation hydrodynamics

In this paper we deal with two types of time-dependent models. One of these is the main simulation whose output we compare with the observations in detail. It was carried out in the course of the present investigation and is referred to as the present simulation. This simulation and the underlying code are described below. The other, older simulation serves to quantify whether changes in the treatment of physical processes, in particular radiative transfer and thermal convection, affect the results. We discuss such a dependence especially for the radiative transfer.

The present simulation treats convection as a completely non-stationary phenomenon, with a system of interacting flows of various scales. We call these models multi-scale (or MS) models.

We also include some results derived with single-scale or steady-state (SS) models to show the influence of temperature fluctuations on the formation of spectral lines. These models treat convective motions as quasi-stationary, cellular and laminar. The resulting convective flows are quasi-stable and cells do not change their horizontal sizes with time. Differences between these two treatments of thermal convection in the outer layers of the Sun were studied in detail by Gadun et al. (1999a).

2.1. System of radiative hydrodynamic equations

In our simulations the medium is described as compressible, radiatively coupled and gravitationally stratified. We neglect the effects of sphericity of the envelope and the influence of molecular viscosity, which we expect to be considerably smaller than turbulent viscosity used. The full system of averaged Reynolds equations is written in the following conservative form (Gadun 1995):

$$\frac{\partial \rho}{\partial t} + \frac{\partial \rho v_j}{\partial x_j} = 0 \,, \tag{1}$$

$$\frac{\partial \rho v_i}{\partial t} + \frac{\partial \rho v_i v_j}{\partial x_j} = -\frac{\partial P}{\partial x_i} - \frac{\partial R_{ij}}{\partial x_j} - \rho g \delta_{i3} \,, \tag{2}$$

$$\frac{\partial \rho E}{\partial t} + \frac{\partial \rho E v_j}{\partial x_j} = -\frac{\partial P v_j}{\partial x_j} - \frac{\partial R_{ij} v_i}{\partial x_j} + \\ + \rho q_D - Q_R - \rho g v_3 \,, \tag{3}$$

where i, $j = 1$ or 3, ρ is the density, v_i is a component of the velocity, E is the total specific energy (i.e., the sum of kinetic and internal energy), P is the total pressure, Q_R represents radiative heating, respectively cooling (see Sect. 2.3) and q_D describes the dissipation of the kinetic energy of averaged motion at the sub-grid level due to the molecular viscosity. Finally, R_{ij} is the Reynolds stress tensor $R_{ij} = \rho \overline{v_i' v_j'}$, or more specifically:

$$R_{ij} \approx \frac{2}{3}\rho(q_t + \sigma e_{kk})\delta_{ij} - 2\rho\sigma e_{ij} \,, \tag{4}$$

e_{ij} is a velocity deformation tensor, q_t is the specific kinetic energy of small-scale ("sub-grid") turbulence, and σ is the kinematic coefficient of turbulent viscosity. We use a simple local gradient model (Smagorinsky 1963) to describe the sub-grid turbulence (cf. Deardorff 1971):

$$\sigma = \frac{2(C_\sigma \Delta)^2}{\sqrt{2}} (e_{ij} e_{ij})^{1/2} \,. \tag{5}$$

In Eq. (4) q_t can be written as $q_t = \frac{1}{2}\sigma^2/(C_\sigma\Delta)^2$, while in Eq. (3) $q_D = C_E q_t^{3/2}/\Delta$. The quantity Δ is the spatial step, $C_E = 1.2$, and $C_\sigma = 0.2$. The constant C_E determines the description of small-scale turbulence and is directly related to the universal constant C in the Kolmogorov spectral law. Since the value of the universal constant C is established experimentally (Monin & Yaglom 1967) it is not difficult to show that C_E has to be close to 1. The constant C_σ = 0.2 is chosen based on the numerical experiments of Deardorff (1972) regarding the simulation of planetary boundary layers and on earlier 2-D grey models of solar granulation (Gadun 1995, Gadun & Vorob'yov 1995, 1996). It can in principle be lower in non-grey atmospheres. We therefore also carried out a series of tests in which we decreased C_σ to 0.05 for otherwise similar parameters of the models and found that, although the dynamic properties of the model flows are changed somewhat, the influence on the temporally averaged line profiles is insignificant.

The ideal gas law is assumed to describe the equation of state. The ionization of hydrogen and the first and second levels of ionization of fifteen other elements are taken into account in LTE. In the low temperature regime ($T \leq 6000$ K), the contributions to the ionization equilibrium of H^- and of the molecules H_2 and H_2^+ are allowed for.

[1] The wavelength shift of spectral lines between the centre of the solar disc and the limb is termed the limb effect.

2.2. Integration of the hydrodynamic equations

To integrate the system of hydrodynamic equations the large particle method is applied (Belotserkovskiy & Davydov 1982). It is a modification of the method of particles in cells (Evans & Harlow 1957) and may be regarded as a fully conservative donor cell scheme with splitting according to physical processes (Roache 1972). This means that each time step of the computations is composed of two steps: the action of pressure gradients and of volume forces is taken into account in the first step, while the transfer effects (convective terms) are calculated in the second step. Upwind differencing was used to approximate the convective terms. The order of the approximation depended on the smoothness of the solution and varied up to second order in regions with a smooth flow.

We note that upwind differencing has a number of physically important properties. For example, a disturbance in some physical value can be transferred only by convection in the direction of the velocity vector (in the absence of diffusion – Roache 1972).

Transsonic flows and shocks are common in dynamic simulations of solar granulation and need to be treated. Two comments on the treatment of shocks are necessary:

1. we use the so called shock-smearing method (Roache 1972) to stabilize a solution near and at a shock. As a result, shocks can be smeared by as much as 3Δ–5Δ, where Δ is the spatial step.
2. Conservative schemes, such as the one used here, are the most suitable to describe shocks (Roache 1972), particularly when applied to the conservative form of the HD equations as presented here. This is because the Rankine–Hugoniot relations are based only on general conservation laws and do not depend on the inner structure of shocks.

2.3. Radiative transfer of energy

The radiative cooling term (Q_R in Eq. (3), the energy equation) is defined as:

$$Q_{R\nu} = \frac{\partial q_{j\nu}}{\partial x_j}, \text{ or } Q_R = 4\pi \int_0^\infty \alpha_\nu \left(B_\nu - J_\nu\right) d\nu \ , \qquad (6)$$

where α_ν and J_ν are the monochromatic opacity and mean intensity, B_ν is the monochromatic source function assumed equal to the Planck function (LTE), and $q_{j\nu}$ is a component of the monochromatic radiative flux.

The radiative energy transfer (needed to find Q_R) is treated in LTE using a differential moments method with variable Eddington factors (Gadun 1995). Within the framework of this approach the complete moments relations can be written for the components of the radiative energy flux vector ($q_{j\nu}$), the mean intensity (J_ν), or directly for the value of radiative heating/cooling ($Q_{R\nu}$). We employ $Q_{R\nu}$, since writing the final expression in terms of J_ν leads to numerical round-off problems at large optical depths (since J_ν tends to B_ν) and the formulation of the radiative transfer equation in terms of the $q_{j\nu}$ gives 2 or 3 final equations, which increases the CPU time.

Assuming that the Eddington tensor has a diagonal form we finally obtain (Atroshchenko & Gadun 1994, Gadun 1995):

$$\frac{\partial}{\partial x_j}\frac{1}{\alpha_\nu}\frac{\partial}{\partial x_j}\frac{f_{\nu jj}Q_{R\nu}}{\alpha_\nu} = 4\pi\frac{\partial}{\partial x_j}\frac{1}{\alpha_\nu}\frac{\partial}{\partial x_j}f_{\nu jj}B_\nu + Q_{R\nu} \ , \quad (7)$$

where $f_{\nu jj}$ are the frequency- and location-dependent Eddington factors. Eddington factors for multidimensional radiative transfer have been previously used by Musman & Nelson (1976) and Hasan (1988), although in these cases the Eddington factors were not variable. The total cooling is given by $Q_R = \sum Q_{R\nu}\omega_\nu$, where ω_ν are the weights introduced by the wavelength discretization. The boundary conditions can be expressed in the form:

$$\frac{1}{4\pi}\frac{\partial}{\partial z}\frac{f_{\nu zz}Q_{R\nu}}{\alpha_\nu} = \frac{\partial}{\partial z}\left(f_{\nu zz} - \frac{1}{3}\right)B_\nu \ , \text{ for } \tau_\nu = \tau_{\nu,\max} \quad (8)$$

and

$$\frac{\partial}{\partial z}\frac{f_{\nu zz}Q_{R\nu}}{\alpha_\nu} = -\alpha_\nu q^0_{z\nu} + 4\pi\frac{\partial}{\partial z}f_{\nu zz}B_\nu \ , \text{ for } \tau_\nu = 0 \ , \qquad (9)$$

where $q^0_{z\nu}$ is the vertical component of the radiative flux at the upper boundary. To determine the Eddington factors and the initial distribution of $Q_{R\nu}$, the transfer equation is solved in 1-D along vertical columns by the Feautrier technique (Mihalas 1978).

A second order scheme is used for the finite difference representation of the equations. To solve the resulting system of algebraic equations an iterative technique is applied.

In the deep, optically thick layers, once the mean free path of a photon drops below 0.1 km, we use the diffusion approximation to find Q_R.

In earlier modeling (e.g., Gadun et al. 1997) the radiative transfer equation was solved in 97 frequency intervals. The absorption by atomic spectral lines was included by using the opacity distribution function (ODF) tables of Kurucz (1979). In the present simulation we use 239 frequency intervals and the ODF tables of Kurucz (1993), which include the opacity due to molecular lines.

Several numerical experiments were carried out to test how different approximations of the wavelength dependence of the opacity influence Q_R (Gadun 1995). The evaluated approximations are:

1. use the grey Rosseland opacity ($\kappa_{\rm R}$),
2. employ monochromatic continuous opacity disregarding line-blanketing effects (κ_ν),
3. add line blanketing through the use of the opacity distribution function (ODF; $\kappa_{\rm ODF}$),
4. include line blanketing through the opacity sampling (OS) method ($\kappa_{\rm OS}$).

In the OS case 556 frequency points were selected and 49035 lines were directly computed. The spectral line parameters were taken from the list of Kurucz (1990).

In the first set of tests we have calculated Q_R using a snapshot from the 3-D models of Gadun (1986, cf. Atroshchenko & Gadun 1994). Five different levels of approximation were used

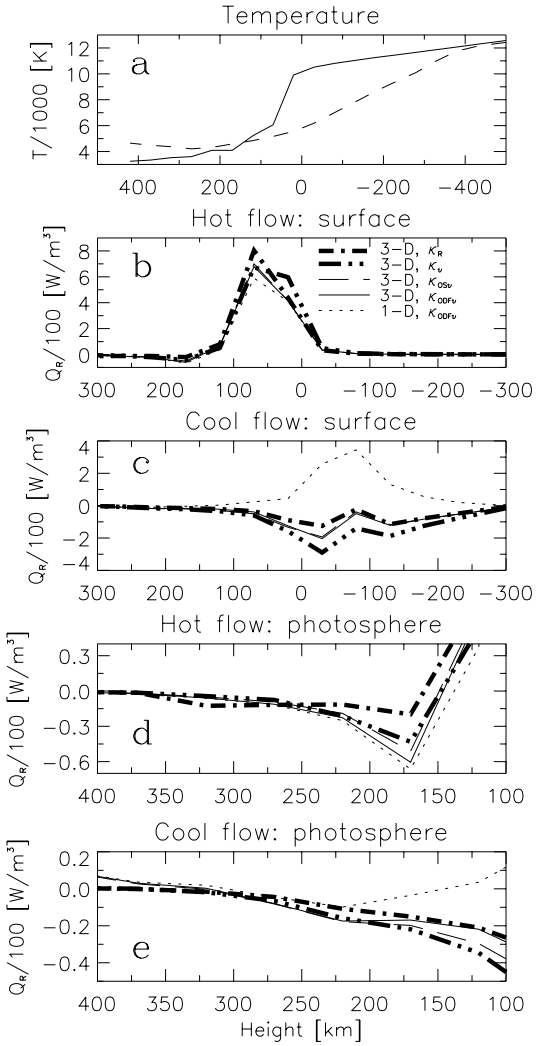

Fig. 1a–e. Height dependence of Q_R, a measure of the radiative heating/cooling, for the centres of an up- and a downflow. **a**: Temperature stratification in the considered up- (solid line) and downflow taken from a 3-D model snapshot (Atroshchenko & Gadun 1994). **b** and **c**: Q_R at the continuum-forming layer for up- **b** and downflows **c**. **d** and **e**: Q_R in the middle and upper photosphere for the centres of up- **d** and downflows **e**. See the text (Sect. 2.3) for additional details

to calculate Q_R, the 4 methods to calculate κ_ν described above, coupled with a 3-D radiative transfer, as well as a fifth one in which $\kappa_{\rm ODF}$ is used, but only a 1-D radiative transfer. The results are plotted in Fig. 1. Fig. 1a shows the temperature stratification along two columns, corresponding to the hottest upflow (solid line) and the coolest downflow in the snapshot. The Q_R values computed for these two columns are given in Fig. 1b–e: in b and c the data are plotted near the solar surface, while d and e show Q_R in the higher-lying photospheric layers. We have plotted all five solutions of Q_R. Positive Q_R corresponds to cooling and negative Q_R to heating.

Consider first the layers near the solar surface of the upflowing column (Fig. 1b): intense emission occurs over a small height range, which is due to a strong temperature dependence of the absorption coefficient in the continuum (basically due to H^- absorption). Solutions for all κ converge in deep layers (Fig. 1b). Differences arise near the continuum-emitting layer. The emission starts earlier in the κ_ν version, which is explained by a smaller number of opacity agents involved in the calculation. The strongest emission occurs when κ_R is used. As $\kappa_{\rm R}$ is a harmonic mean, the frequencies at which the opacity is the least and the emission the strongest enter it with the largest weight. Thus, the use of $\kappa_{\rm R}$ leads to a more effective radiative cooling. The values of Q_R obtained with $\kappa_{\rm ODF}$ and $\kappa_{\rm OS}$ are in good mutual agreement. When the radiative transfer is considered in 1-D only, the radiative cooling diminishes because radiation losses are insufficiently taken into account.

The situation is rather different in cool downflows (Fig. 1c). They are radiatively cooled if 1-D transfer is considered, but when the multidimensionality of the medium is allowed for, they are heated owing to the emission from neighbouring hot upflows. The least amount of heating occurs in the grey atmosphere with the Rosseland mean absorption coefficient. This is because $\kappa_{\rm R}$ "underestimates" the frequencies at which the absorption is largest and where, therefore, the heating is greater. The greatest heating is found with κ_ν, since the medium is more transparent for the emission from neighbouring hot regions. The agreement between results based on $\kappa_{\rm ODF}$ and $\kappa_{\rm OS}$ is again excellent.

In the upper photosphere (Fig. 1d) the radiative cooling above granules (i.e. in upflows) gives way to heating (at $h \approx$ 170 km), since the upflows become cooler here than the ambient medium (see Fig. 1a). In the height range 100–300 km Q_R calculated using $\kappa_{\rm OS}$ differs from that resulting from the use of $\kappa_{\rm ODF}$ (in both columns). Above granules the radiative heating is somewhat smaller for $\kappa_{\rm OS}$ into whose calculation a lesser number of lines enters as compared with $\kappa_{\rm ODF}$. The heating is basically one-dimensional in nature – it is produced by radiation propagating from below the same "granule". Hence, the 1-D and 3-D solutions yield similar results. Along downflows in the upper photosphere (Fig. 1e) the matter is hotter than above "granules" (upflows, cf. Fig. 1a), and it cools when line absorption is taken into account. Temperature fluctuations in the photosphere are thus smoothed out. The influence of the line haze in the upper photosphere may be overestimated in our treatment, since we do not take into account scattering by lines contributing to the haze (see, e.g., Nordlund 1985).

These calculations demonstrate the importance of a detailed treatment of radiative energy transfer, with the usage of either OS or ODFs to treat line blanketing. Both approximations lead to similar results. This inference can be regarded as a test of the used ODF table, because some of the assumptions on which the ODF concept is based can be a source of serious errors (Gustafsson et al. 1975). We shall return to this point again in Sect. 2.6.

In the second set of experiments, we calculated four sets of 2-D models with a 1-D and 2-D treatment of radiative transfer, each using $\kappa_{\rm R}$ or $\kappa_{\rm ODF}$. The results of these experiments are described in Sect. 2.6.

2.4. Boundary conditions

The lower and upper boundaries are open, i.e., free inflow and outflow of matter is permitted. Nevertheless, further constraints need to be imposed.

In the present simulation the condition $\partial \mathbf{v}/\partial z = 0$ is imposed on the velocity at the upper and lower boundary, while the mean internal energy and density are required to remain on average at the values set by the initial conditions. They are, however, allowed to fluctuate around these mean values. Their fluctuation profiles at the upper boundary are made to fit the underlying layer, while at the lower boundary they are chosen to correlate with the vertical velocity fluctuation profile – hotter and less dense matter should ascend. The density at the lower boundary is also scaled in order to provide a constant pressure at the lowest horizontal level.

At the lower boundary we additionally scale the density of those flows entering the domain in order to satisfy mass balance at each time step (Atroshchenko & Gadun 1994). At the top, we postulate that the matter entering the domain is in hydrostatic equilibrium and that its initial velocity outside the domain is equal to zero. This corresponds to postulating that a part of matter lying outside the upper boundary of our domain is stable and doesn't take part in oscillations.

At the lateral boundary periodic conditions are chosen.

2.5. General properties of the 2-D models

The present computations were carried out in a box with dimensions 3360×1960 km. Atmospheric layers occupy about 700 km in these models. The spatial step was 28 km in both directions. The simulation ran for a total of $2^h\ 27^m$. Spectral lines were calculated using the last 255 models, with a 30 s time step between them.

The initial conditions were chosen in such a way as to treat thermal convection as a non-stationary process with evolving and interacting convective flows (MS modeling). Oscillatory motions are directly excited in the models. They are important in the middle and upper photospheric layers, where they significantly impact on the dynamic state of the gas.

The upper limit of the theoretical Reynolds number in the models may be estimated as (Orszag 1977) $Re \sim (L/\Delta x)^{4/3} \sim 590$, where L is the horizontal size of the modeled region and Δx is the spatial step.

In Fig. 2 we show the temporal evolution of flows over a period of 10 min in steps of 2.5 min. Regions with Mach numbers greater than 0.9, 1.0 and 1.2, respectively, are identified by increasingly darker shading. Supersonic vertical velocities in the upper atmosphere, supersonic horizontal velocities in the photosphere, and supersonic downflows near and under the visible surface are clearly seen.

The presence of flows in excess of the local sound speed is in agreement with the results of the 2-D and 3-D simulations by Cattaneo et al. (1989), Malagoli et al. (1990), Steffen & Freytag (1991), Rast et al. (1993) and Stein & Nordlund (1998).

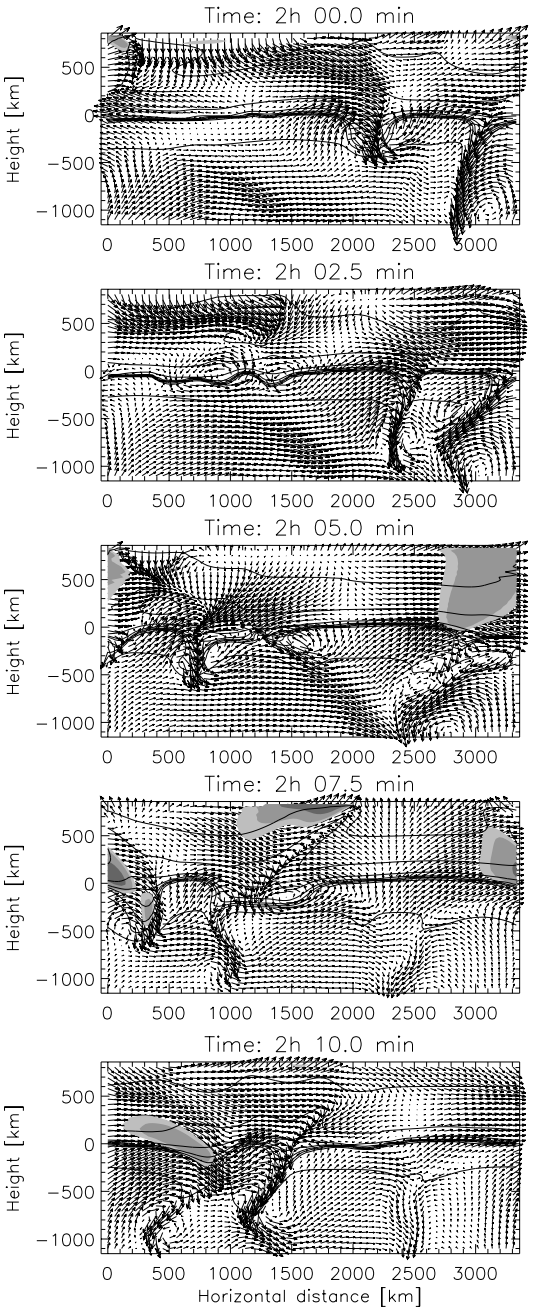

Fig. 2. Temporal evolution of velocities (denoted by vectors) and temperature (isotherms). Time increases by 2.5 min between consecutive frames (from top to bottom). Horizontal lines are isotherms corresponding to T = 4000, 5000, 6000, 7000, 8000, 9000, 10000 and 12000 K (from top to bottom in each frame). Regions with Mach number larger than 0.9, 1.0, and 1.2 are shaded increasingly heavily. The flow vectors are normalized separately for each frame

For illustrative and comparative purposes we have also determined the relevant parameters from 2-D SS models (Gadun 1995, Gadun et al. 1997). The size of the modeled region in this case was 1295×2030 km in the horizontal and vertical directions. The spatial grid size was 35 km. A snapshot of one such model is shown by Gadun et al. (1997). Although

they are in many respects less realistic than the other models we shall nevertheless also compare these models with the observed intensity fluctuations in the continuum and line cores because they have temperature fluctuations similar to those obtained from semi-empirical investigations (Altrock 1976, Keil & Canfield 1978, Kneer et al. 1980).

2.6. SS models: self-consistency of the velocity field and the temperature distribution

In order to show how the treatment of radiative transfer affects the simulations, we calculated sequences of SS models with five different treatments of the radiative transfer: 1-D and 2-D in combination with $\kappa_{\rm R}$ and $\kappa_{\rm ODF}$, respectively. $\kappa_{\rm ODF}$ was calculated using the ODFs of Kurucz (1979). 97 separate frequency intervals are considered and the influence of molecular lines was neglected. The fifth set of SS models was obtained with 2-D radiative transfer and $\kappa_{\rm ODFmol}$ – i.e., using monochromatic opacities in 239 frequency bins and considering also molecular lines (ODFs of Kurucz 1993). In many aspects the results of this fifth set of models are very close to the 2-D, $\kappa_{\rm ODF}$ case. For this reason we show only some of these results.

In the 1-D case only vertical rays were considered. Each of the five model sequences was run for nearly 1 h of solar (hydrodynamic) time.

Fig. 3a displays the temperature stratifications of the four models averaged over time and over horizontal layers. The average temperature obviously depends primarily on the representation of the absorption in the medium and only secondarily on the dimensionality of the radiative transfer. Interesting is a comparison with plane-parallel hydrostatic atmospheres. When line blanketing is taken into account in one-dimensional plane-parallel hydrostatic LTE model atmospheres, the temperature drops in the outer layers, due to line cooling, and rises in the deeper layers due to the back-warming effect. Inclusion of line absorption in multidimensional HD solar model atmospheres produces somewhat different results. Allowing for additional absorption at the frequencies of spectral lines permits hot adiabatic upflows to overshoot still further into the photospheric layers, emergent radiation to heat the matter in the middle photosphere and to smooth temperature fluctuations in the upper photospheric layers (Sect. 2.3). Hence, the upper photosphere of hydrodynamic models can be hotter than hydrostatic models. This effect is independent of whether the radiative transfer is 1-D or 2-D (Fig. 3). We also note the existence of back-warming, although by a small amount, in the models calculated with line absorption. The influence of line blanketing has also been discussed by Nordlund (1985), Rutten (1988), and Nordlund & Stein (1991).

The average temperature in the photosphere is found to be higher for 2-D grey radiative transfer than for 1-D (Fig. 3a). Basically, this is because 2-D transfer facilitates the energy exchange between structures and makes the horizontal temperature distribution more smooth, thus permitting the residual convective motions to overshoot more energetically into stable photospheric layers and reduce the photospheric oscillations.

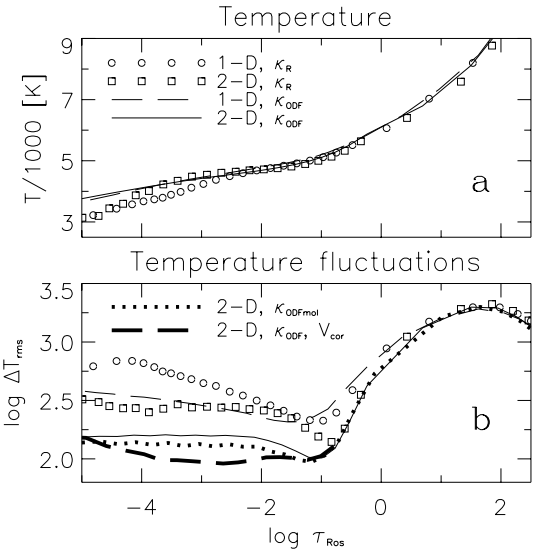

Fig. 3a and b. Mean temperature stratification **a** and temperature rms fluctuations **b** in sets of test models incorporating different treatments of the radiative transfer. Their detailed description is given in the text. Thick long dashes in **b** are the results of calculations with special upper boundary conditions (see text). The data were averaged horizontally and over time

However, it is significant that the spatial averaging of the radiation field has almost no effect on the mean temperature profile in the upper model layers with $\kappa_{\rm ODF}$ (Fig. 3a). The reason is that in these atmospheric layers the radiative heating of upflows is basically one-dimensional in nature (see Sect. 2.3).

Importantly, however, the temperature fluctuations (Fig. 3b) strongly depend on both the radiative transfer treatment and on the velocities in the upper part of the computational domain. To demonstrate this we ran a simulation for 20 min solar time with 2-D radiative transfer employing ODFs, but now artificially imposing that above 350 km in the atmosphere all horizontal velocities are less than 1.5 km s^{-1} and vertical velocities lie below 2.5 km s^{-1}. In Fig. 3b the rms temperature fluctuations resulting from these calculations are shown by the thick long dashed lines. They are lower than in the case of free boundary conditions and are at the 100 K level almost throughout the photosphere. Note that the introduction of additional opacity sources ($\kappa_{\rm ODFmol}$) also reduces the temperature fluctuations.

The velocity field patterns corresponding to the 5 cases discussed above are shown in Fig. 4. The atmosphere can be arbitrarily divided into three regions according to the vertical velocity field: the layer of convective velocities in the lower photosphere, the layer of photospheric overshooting convection (corresponding to the layers with the smallest vertical velocity amplitude), and the layer of increased vertical velocity associated with the excitation of oscillations and waves. The impact of the wave-component is stronger for cool models with grey atmospheres, and the oscillatory velocity amplitudes are larger for 1-D radiative transfer. The effect of the angular averaging of the radiation field is stronger than that of the description of

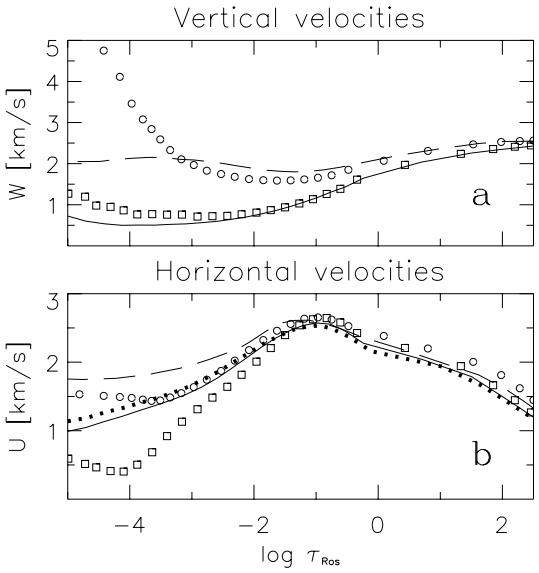

Fig. 4a and b. Stratification of rms vertical **a** and horizontal velocities **b** averaged over horizontal layers and in time for five sequences of 2-D models. Designations are the same as in Fig. 3

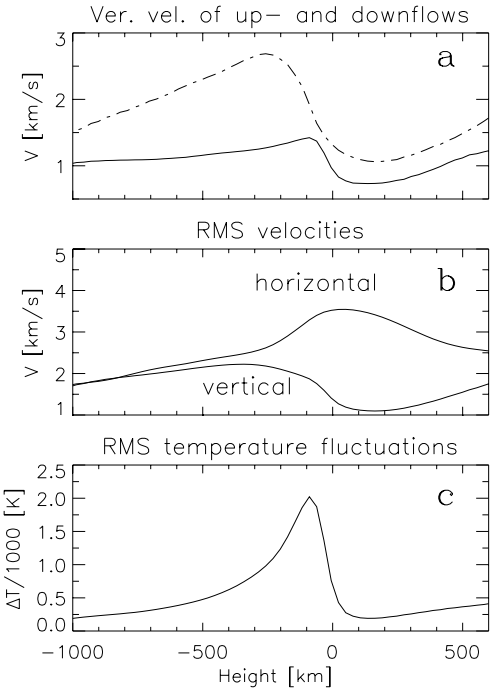

Fig. 5a–c. Stratification of components of velocity field and rms temperature fluctuations in the present models. **a** Vertical velocities averaged over up- and downflows separately. The solid and dash-dotted lines represent up- and downflows. **b** RMS horizontal and vertical velocities. **c** RMS temperature fluctuations

the absorption coefficient. The latter mainly plays a role in the upper photosphere.

Grey models with 1-D radiative transfer are characterized by extremely cool convective downflows. This and the low level of radiative damping leads to the large oscillations, in agreement with Gadun et al. (1999a) who showed that convective downflows (plume-like structures), especially if they are supersonic and pulsed, are sources of local acoustic waves in the photosphere.

In summary, the temperature stratification and the velocity field pattern depend on both the angular averaging of the radiation field (i.e., whether the radiative transfer is 1- or 2-D) and the description of the absorption coefficient as a function of frequency. All in all the multidimensionality of the radiative transfer is more essential, although the frequency dependence of the absorption coefficient (including line absorption) also has a considerable influence. Going from 1-D to 2-D reduces the velocity amplitude and temperature fluctuations, while a non-grey absorption coefficient decreases temperature fluctuations and affects the interaction between the wave and convective contributions to the velocity field in the upper photosphere.

2.7. MS models: velocity field and fluctuations of thermodynamic quantities

In this section we analyze briefly the basic properties of the present simulation. Similar 2-D models were studied in detail by Ploner et al. (1998, 1999) and Gadun et al. (1999a).

The surface level in all the plots in this section corresponds to $\log \overline{\tau_R} = 0$, where $\overline{\tau_R}$ is the spatially and temporally averaged Rosseland optical depth.

Fig. 5a displays unsigned vertical velocities averaged separately over up- and downflows. In agreement with previous simulations the downflows are more rapid in all layers, but particularly in the subsurface layers, due to the different areas covered by up- and downflows. RMS horizontal and vertical velocities are given in Fig. 5b. Finally, rms temperature fluctuations are plotted in Fig. 5c.

The present models display, in addition to the well-known reversal of the temperature fluctuations in the lower photosphere (i.e. at heights $\gtrsim$ 170 km the upflows above the granules are cool, while the downflow lanes are hot), a second reversal in the upper photosphere. Above this second reversal upflows are hot and downflows cool. Note that the reversal is in the correlation between temperature and velocity fluctuations at the same horizontal level. At a given horizontal location the sign of the fluctuation in temperature or velocity does not need to change at this height, however. Hence the upper reversal does not imply that the granular pattern is visible in the upper photosphere. The reversal is illustrated in Fig. 6 in which the difference between the temperature stratifications averaged over the up- and downflows and the temperature averaged over the whole horizontal extent of the domain is plotted. Note the two heights at which the two temperature fluctuation curves cross each other. The reversal at 170 km results from the radiative and expansion-related cooling of upflowing material, and from compression-induced heating of the downflows. The higher-lying reversal is due to the fact that in the upper photosphere oscillations become increasingly important, so that their phase relationship dominates.

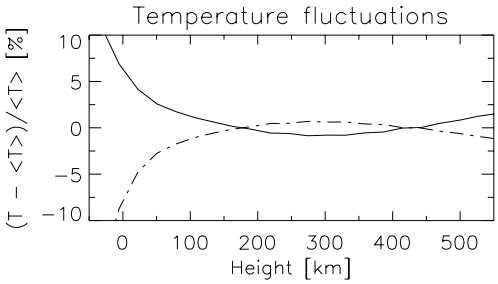

Fig. 6. Stratification of relative temperature fluctuations of up- and downflows. Solid line represents upflows and dash-dotted line shows downflows

2.8. Expected limitations of the simulations

Our 2-D LTE approach to studying the problem of solar granulation has limitations that have to be borne in mind when analysing the model results. These are outlined below.

1. Partly these limitations are due to the restriction to two spatial dimensions (in cartesian geometry), whereas granulation is known to be a 3-D phenomenon. The reasons for choosing this restrictive setting were outlined in the introduction. Here we point out two consequences.

a) As will be discussed in detail by Solanki et al. (in preperation) the relationship between vertical and horizontal convective velocities is different in 2-D and in 3-D, as imposed by mass conservation. This effect also influences the thermal fluctuations, in particular in the upper atmosphere. Therefore, we expect synthetic line profiles resulting from 2-D simulations to differ from those resulting from 3-D models.

b) In 2-D both energy and enstrophy (a measure of vorticity) are conserved, whereas in 3-D enstrophy may change. Let us call the scales on which vorticities dissipate and on which the turbulent flow is generated l_d and l_g, with $l_d \ll l_g$. Then, in the spatial wavenumber range $2\pi/l_g < k < 2\pi/l_d$ in 2-D turbulent flows no energy flux will be transferred over the spectrum of kinetic energy from large to small scales, in contrast to 3-D turbulence, while a vorticity flux from large to small scales is present. At large scales ($k < 2\pi/l_g$, i.e. near the basic scale of instability which produces the 2-D turbulence, e.g., driven by thermal flows), on the other hand, the theory of 2-D turbulence (Mirabel & Monin 1979) predicts the opposite situation: kinetic energy is transferred from smaller to larger scales while vorticity transfer is absent. Formally, however, in this range the spectrum of kinetic energy is the same as in 3-D, i.e., $E(k) \sim k^{-5/3}$, so that we can expect there to be more energy in large-scale inhomogeneities in 2-D than in 3-D.

c) In 3-D thermal convection there is a large topological asymmetry between up- and downflows at the solar surface (Cattaneo et al. 1989; Spruit et al. 1990): downflows are always connected ("dark" intergranular lanes form a multiply connected network) while upflows are isolated. In 2-D absolute topological symmetry exists for both kinds of flows, for obvious reasons. It is not yet clear in which way such a difference can influence the final comparison of spectral line computations with observations.

d) Horizontally rotating vortices of different size can form in 3-D simulations (Nordlund & Dravins 1990, Stein & Nordlund 1998). It is possible that these affect absolute line shifts, although calculations to test this still need to be carried out.

2. Another limitation lies in the treatment of radiative transfer. It is important to take into account molecular lines in detail, foremost among them infrared vibration-rotation bands of CO. They may play an active smearing role for the temperature fluctuations in the upper photosphere (cf. the calculations of Steffen & Muchmore 1988, which, however, were of a quasi steady-state type). In addition, NLTE effects may become significant in the upper model atmosphere as was shown by Nordlund (1985, cf. also Rutten 1988).

The use of ODFs can also lead to some inaccuracy in the energy balance in the model atmosphere, since it is assumed that within a certain spectral interval the same lines predominate through the entire depth in the atmosphere. Errors may also arise owing to the choice of points dividing the spectrum into wavelength intervals and to the small number of sampling bins within each ODF interval (Gustafsson et al. 1975). These errors may be negligible when the ODF tables are constructed in a corresponding manner, as demonstrated by Gustafsson et al. (1975). Nevertheless, even small absolute differences in the final temperature structure of the models may result in substantial differences in the spectral lines synthesized from these models, since some lines are strongly sensitive to the temperature gradient.

Near the visible solar surface all our models have similarly large $\Delta T_{\rm rms}$, producing high continuum intensity fluctuations. At λ 5000 Å our SS models show an intensity rms of about 20–22%, while our MS models exhibit 22–24% (Gadun 1995, Gadun et al. 1997). These values are similar to those found by Steffen (1991) and Lites et al. (1989, for the models of Stein et al. 1989).

3. Observations and reduction

We used the 26-inch telescope and the Coudé Littrow spectrograph of the Big Bear Solar Observatory (BBSO) to obtain most of the data discussed in this paper. The data set, which was obtained on June 30, 1995, consists of a sequence of digital spectra of quiet Sun obtained at 3 different heliocentric angles $\theta = 60°$, 65° and 70°, corresponding to $\mu = 0.5$, 0.42 and 0.34. A total of 56 frames were recorded, 23, 16 and 17 frames at the three μ values, respectively. The slit was placed parallel to the solar limb. The detector was a 1024×1024 pixels CCD camera, but 2×2 pixels were binned in order to increase the signal-to-noise ratio. The effective image scale and dispersion after binning are 0.2 arcsec/pixel and 1.4 pm/pixel. The exposure time per image was 0.5 s.

The spectral region considered contains the Ni I line at λ 4912 Å, which has no magnetic sensitivity. The data were reduced in the usual manner (dark current subtraction, flat fielding, etc.) and the spectrum of Ni I 4912.0 Å was extracted at each spatial location. The further analysis of the observed spectra is almost identical to that of the synthetic spectra emerging from

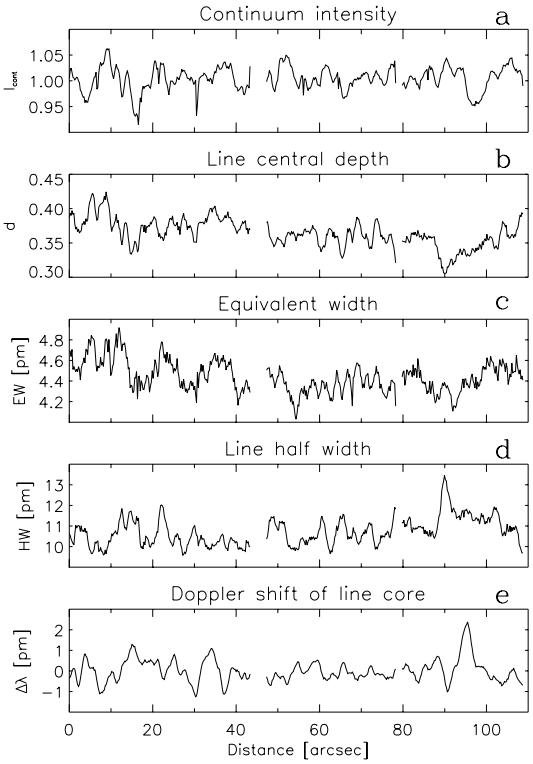

Fig. 7a–e. Example of line parameters observed at μ = 0.5. Plotted are **a** the continuum intensity I, **b** line central depth d, **c** equivalent width EW, **d** line half width HW and **e** Doppler shift $\Delta\lambda$ along the slit

the hydrodynamic models and is described in detail in Sect. 4. In brief, the line depth and line width are determined from a Gaussian fit to the lower part of the line profile. The line shift along the slit is first detrended using a second order polynomial. The line width (FWHM) and equivalent width are also determined. The continuum window chosen is centered on a relatively clean area of the spectrum just redward of the line.

Samples of various parameters of spectra observed at μ = 0.5 are shown in Fig. 7.

It should be noted that stray light in combination with difficulties in obtaining a good flat field lead to uncertainties in the absolute measurements of line depth and equivalent width. We therefore use these measurements only in a relative sense. They cannot be compared directly with measurements corrected for such effects.

In addition to these data we also analysed a set of Fe I and Fe II spectral lines taken from the Jungfraujoch atlas (Delbouille et al. 1973), which correspond to low spatial-resolution observations at $\mu = 1$. More details on these lines are given in Sect. 4.

4. Line computations

Two sets of line computations have been carried out, one encompassing a set of Fe I and Fe II lines taken from the list of Atroshchenko & Gadun (1994). The synthetic bisectors and wavelength shifts of these lines are compared with corresponding values taken from the Jungfraujoch atlas and the compilations of Dravins et al. (1981, 1986), respectively. To this end we have computed 10 Fe I and 7 Fe II lines in the SS and the present MS models.

In addition, the Ni I 4912 Å line has been synthesized in the MS model across the solar disc at μ = 1.00, 0.85, 0.7, 0.5, 0.42 and 0.34, and compared with our high spatial resolution observations. To help understand the results of this line additional Fe I lines were also calculated (see below).

All synthetic lines were calculated in LTE along vertical or inclined rays which pass through the given model atmosphere. The horizontal spatial positions of these rays coincide with computational grid-points at the upper boundary of the computational domain. At the other heights the corresponding model quantities were linearly interpolated onto these rays.

The centre-to-limb variation of correlations between parameters of a spectral line (for instance, Ni I 4912.03 Å) is expected to be the result of a variety of influences:

1. A height dependence of the corresponding correlations.
2. The different visibility of vertical and horizontal velocity components at disc centre and near the limb.
3. The different visibility of small-scale structure at different disc locations. For example, if cool gas overlies the hot regions in the lower photosphere, and hot gas overlies cool regions, then at disc centre line core brightness (formed in the upper photosphere) and continuum intensity (lower photosphere) will show a strong anti-correlation. Sufficiently close to the limb, however, due to parallax effects the hot upper-photospheric structure may lie in front of hot lower-photospheric features, so that the correlation could now reverse and become positive. This effect is expected to be important only for the smallest granules.

The influence of the height dependence can be separated from the rest by considering a sample of lines formed at different heights at the centre of the disc. Such height-dependent variations should be clearly present because the lower and upper layers of the solar photosphere are controlled by different physical processes, namely by overshooting convection and by oscillations, respectively. Hence we selected a set of Fe I lines whose effective formation levels evenly cover the whole height range of our model atmospheres.

In this list of synthesized lines – given in Table 1 – we included several Fe I lines employed for high spatial resolution observations by Hanslmeier et al. (1990, 1994). In Table 1 line wavelengths (λ) and lower excitation potentials (EPL) are taken from Moore et al. (1966); $d_{\rm ob}$ and $W_{\rm ob}$ are the central depth and equivalent width obtained from the Liège atlas (Delbouille et al. 1973); $\log\tau_{5W}$ and $\log\tau_{5d}$ are the effective optical depths of formation at λ 5000 Å for the equivalent width (i.e., weighted mean over the whole profile) and for line centre, respectively; H_W and H_d are the corresponding effective geometrical heights of formation. The $\log\tau_{5W}$ and $\log\tau_{5d}$ values were determined with the line depression contribution function and the Unsöld-Pecker weighting function (Gurtovenko et al. 1991, Gadun & Sheminova 1988) using the quiet-sun model of Holweger & Müller (1974). Note that all line parameters of the

Table 1. Parameters of the calculated spectral lines

λ Å	El.	EPL eV	$d_{\rm ob}$	$W_{\rm ob}$ mÅ	$\log\tau_{5d}$	$\log\tau_{5W}$	H_d km	H_W km
4911.536	Fe I	4.26	0.268	24.	-1.05	-0.87	163	134
6494.499	Fe I	4.73	0.261	31.5	-1.16	-0.95	179	146
6495.740	Fe I	4.83	0.344	39.1	-1.28	-0.97	199	150
4911.782	Fe I	3.93	0.493	44.	-1.37	-1.07	214	166
4912.025	Ni I	3.77	0.522	53.	-1.42	-1.13	222	175
5679.032	Fe I	4.65	0.556	64.6	-1.65	-1.13	259	176
6496.472	Fe I	4.79	0.521	67.7	-1.75	-1.18	276	183
5543.944	Fe I	4.22	0.603	67.1	-1.82	-1.25	286	195
6027.059	Fe I	4.07	0.597	66.4	-1.99	-1.31	315	204
6481.878	Fe I	2.28	0.573	63.9	-2.21	-1.62	348	253
6280.622	Fe I	0.86	0.612	62.1	-2.50	-1.82	394	287
5250.216	Fe I	0.12	0.710	64.9	-2.70	-2.02	426	318
5250.654	Fe I	2.20	0.793	103.5	-3.31	-2.09	520	327
6494.994	Fe I	2.40	0.753	162.	-4.16	-2.12	656	332

synthesized profiles were evaluated relative to the local continuum.

In order to compare the CLV of Ni I 4912 Å with lines formed deeper in the atmosphere we executed analogous centre-to-limb computations for the weak Fe I 4911.54 Å line.

The quantity Agf (the product of the abundance with the oscillator strength) for each line was found from computations at disc centre by fitting the synthesized central line depth (taken from the line profile averaged over time) to the Liège atlas value (Delbouille et al. 1973). Van der Waals broadening was taken into account in the approximation of Unsöld (1955). The correction factor of $E_\gamma = 1.5$ to the Van der Waals and the Stark broadenings was estimated on the basis of 3-D HD models (Atroshchenko & Gadun 1994).

To simulate the finite spectral resolution of the observations we convolved the synthetic profiles with a Gaussian having a dispersion of 20 mÅ. The limited spatial resolution of our observations was modeled by a point-spread-function having the form of the sum of two Lorentzians (Nordlund 1984a). For their parameters we chose 2 different sets of values. The first set corresponds to the one already employed by Nordlund (1984a): $a_1 = 180$ km, $a_2 = 1800$ km, with weights of 0.6 and 0.4, respectively (this point-spread-function is hereafter called PSF1). The second set (referred to as PSF2) has the values: $a_1 = 235$ km, $a_2 = 2000$ km, and the weights 0.4 and 0.6. These values result from a fit to our observed continuum intensities near the solar limb (see Sect. 5.3). We also carried out extensive calculations with Gaussian point-spread-functions of different widths, but these were far less successful than the sums of 2 Lorentzians in reproducing the observed CLV of the rms of continuum intensity (cf. Sect. 5.3).

Finally, when comparing with the low spatial and temporal resolution Jungfraujoch atlas we averaged the synthetic spectra both spatially over the whole horizontal simulation domain and temporally.

5. Results of line computations

5.1. Analysed line parameters

The synthesized lines described in Sect. 4 are analysed in different ways. We are interested in both, averaged properties of spectral lines, as well as their dependence on time and spatial location. To study the former the traditional parameters such as spatially and temporally averaged line bisectors and shifts are considered (see Sect. 5.2), while for the latter we employ statistical methods. We describe the analysis of the rms of intensity values in Sects. 5.3 and 5.4, and correlations between spatial fluctuation of parameters in Sects. 5.5 and 5.6.

The spatially averaged wavelength shift of the line core and the line bisector are considered mainly at disc centre. In addition to the direct comparison of bisectors resulting from simulations and observations we also parameterized the bisectors to allow a simpler representation and the comparison of many spectral lines with the observations. We call this parameter ΔV. It represents a wavelength difference in velocity units. If the bisector has a 'C' shape then ΔV is the wavelength difference between the bluemost wavelength of the bisector and the line core. If the bisector is not 'C'-shaped, i.e. bisector wavelength and intensity are monotonically related, then ΔV is proportional to the difference between the wavelength of the bisector at the intensity level 0.97 and the line core. These parameters were also determined from the corresponding line profiles taken from the Jungfraujoch atlas (Delbouille et al. 1973).

In addition to these spatially averaged quantities we have considered the spatial variation of a number of line parameters. Following Hanslmeier et al. (1994) we determined 10 correlation coefficients between the spatial variations of the following parameters: Doppler velocity in the line core (δv; the δ represents spatial variation), the residual intensity at line centre (δr), the half-width of the line profile (δHW), its equivalent width (δEW), and the continuum intensity (δI). Following spectroscopic tradition the line-of-sight velocity directed away from the observer is positive. Both the observed high spatial resolution and simulated spectra were treated in the same manner.

For the observational data the correlations were computed in two ways. In the first method the line and continuum parameters from all slit positions, respectively time steps (both of which we shall collectively refer to as "scans" in the following) were collected and correlated. In the second method the correlations between parameters were determined for each scan and mean correlation coefficients were obtained by averaging over all scans. Both methods give very similar results. The differences in correlation coefficients do not exceed approximately 0.01.

For the simulated spectra the same correlations as for the observations were determined at each time step. The mean values of the correlation coefficients were then averaged over time. For $\mu \neq 1$ we found that the averaged correlations depended slightly on whether the rays crossed the model region from left-to-right or from right-to-left. This is caused by the presence of the shearing instability. Therefore, we additionally averaged the

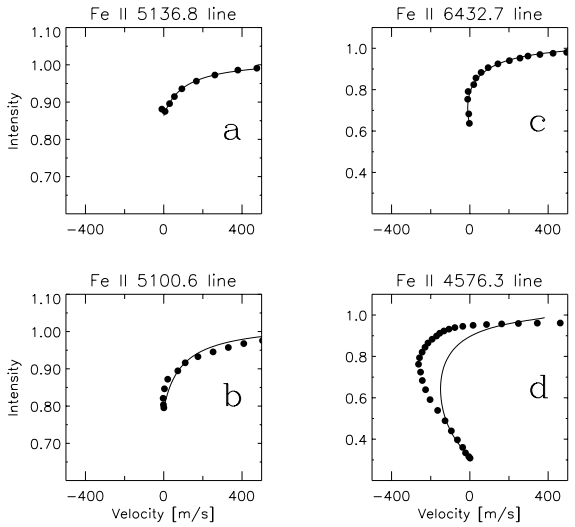

Fig. 8a–d. Comparison between the line bisectors of computed and observed spectral lines. Observations are shown by dots, bisectors of synthesized lines are given by solid lines

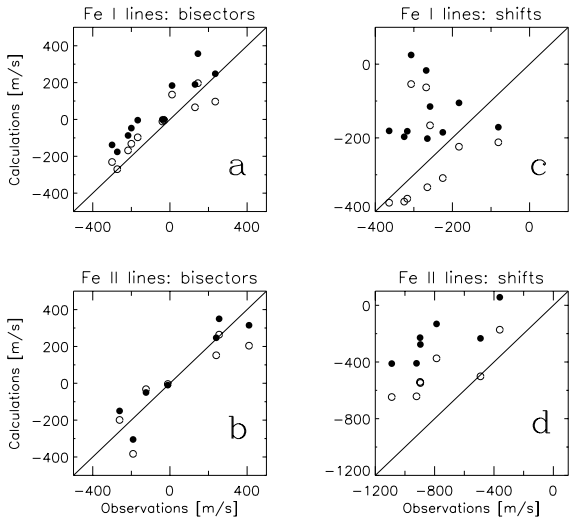

Fig. 9a–d. Parameterized bisectors **a** and **b** and absolute shifts in m s^{-1} **c** and **d** of the computed spectral lines vs. those of the observed Fe I and Fe II lines. Open circles denote spectral lines computed with SS models, filled circles display computations with the present MS models

theoretical correlation coefficients resulting from the spectral simulations with positive and negative θ.

Thus, to obtain the correlation coefficients between the line parameters we used the complete sample of high resolution observational and theoretical data. A similarly extensive, but purely observational study was earlier carried out by Hanslmeier et al. (1990) using several lines observed near disc centre, allowing us to compare our theoretical correlations with their results.

5.2. Line shifts and bisectors at disc centre

Examples of bisectors of spatially and temporally averaged line profiles are shown in Fig. 8 in addition to the observed bisectors, obtained from the atlas of Delbouille et al. (1973). The Fe II lines have been selected due to their low sensitivity to NLTE effects (Solanki & Steenbock 1988, Rutten 1988, Rutten & Kostik 1988).

The observed and computed ΔV parameters describing the bisectors of Fe I and Fe II lines (see Sect. 5.1) are compared in Figs. 9a and b, respectively.

According to Figs. 9a and b both the MS and the SS models reproduce the observed bisector shapes approximately equally well. The bisectors of most lines produced by the MS models demonstrate a deficit of blue asymmetry, which is in general associated with the hot upflows (cf. Gadun et al. 1997).

Simulated and observed absolute line shifts are compared in Figs. 9c and d. The observed values were taken from the papers of Dravins et al. (1981, 1986). The comparison reveals that the models give a deficient blue shift in particular for Fe II lines, but also to a certain extent for Fe I lines. Single-scale 2-D models display a somewhat better agreement with the observed line shifts.

At the same time, calculations even with single-scale 2-D models give underestimated blue shifts for Fe II lines which are formed deep in the photosphere. The blue absolute shifts of most Fe II lines do not appear to exceed about $\sim$650 m s^{-1} in Fig. 9d. From the multi-scale model data this limit can be estimated as $\sim$400 m s^{-1} (for these lines). This discrepancy is not due to insufficient spatial resolution of the numerical simulations near the continuum-forming layer. This is demonstrated by a MS test model with a spatial step of 15 km, using the same computational domain. The finer grid slightly improved the agreement, but the main differences still remain.

The analysis of Bellot Rubio et al. (1999) and Frutiger et al. (1999) suggest that this considerable discrepancy is to at least a large part due to error in Fe II laboratory wavelengths, which are systematically too small. Hence the observed blueshifts are overestimated.

It is thus unclear whether the actual line bisectors and shifts are better reproduced by the SS models or by the MS models. In any case the SS models are far inferior in reproducing correlations between line parameters (Gadun et al. 1997), producing far larger values than both the observations and the MS models.

5.3. Fluctuations of continuum intensity

The rms intensity fluctuations in the continuum are probably the best indicator of the spatial resolution of observations. In addition, intensity fluctuations in various lines allow us to investigate how temperature fluctuations change with height in the photosphere. In this section we consider continuum intensity fluctuations and deal with line core fluctuations in Sect. 5.4. The relative rms fluctuations of continuum intensity ($\delta I_{\rm rms}/\overline{I}$) are plotted in Fig. 10a as a function of μ and in Fig. 11a vs. wavelength.

According to Fig. 10a $\delta I_{\rm rms}/\overline{I} \approx 2\%$ in our observations, with little dependence on μ. This value is smaller than those published by Pravdjuk et al. (1974). They obtained $\delta I_{\rm rms}/\overline{I}$ at an effective wavelength of $\lambda\,5000$ Å using a stratospheric balloon-

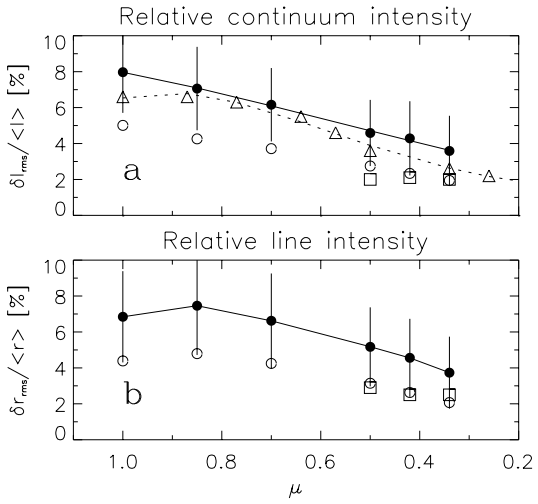

Fig. 10a and b. Relative rms intensity fluctuations in the continuum and in the line core as a function of $\mu = \cos\theta$, where θ is the heliocentric angle. Error bars represent estimates of the standard deviation. **a** Relative rms fluctuations of the continuum intensity. Dots are the simulated values at λ 4912 Å smoothed by the point spread function of Nordlund (1984a; PSF1), open circles are values obtained after smearing by PSF2 – a modified (broadened) form of PSF1. Open squares are the present observations. Open triangles are the balloon borne observations described by Pravdjuk et al. (1974). **b** Relative intensity fluctuations in the core of Ni I 4912.03 Å. Designations correspond to **a**

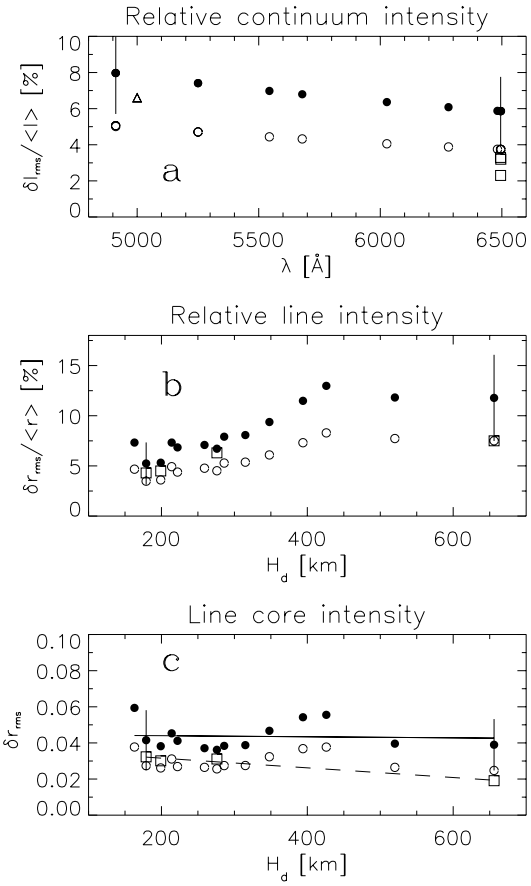

Fig. 11a–c. Intensity fluctuations in the continuum and in line cores as a function of wavelength and height. **a** Relative rms fluctuations of the continuum intensity as a function of wavelength at $\mu = 1$. Dots and open circles are the values resulting from the present 2-D models after smearing by PSF1 and PSF2, respectively. Error bars are estimates of standard deviations. Squares are the observations of Hanslmeier et al. (1990) and the open triangle represents the balloon-borne observations of Pravdjuk et al. (1974). **b** Relative rms intensity fluctuations in the cores of the spectral lines listed in Table 1, vs. the height of formation of their cores. Designations correspond to **a**. **c** Absolute rms intensity fluctuations in units of residual intensity for the cores of lines given in Table 1. Symbols correspond to **b**. The solid line is a linear fit to the filled circles, the dashed line to the observations of Hanslmeier et al. (1990)

borne telescope (open triangles in Fig. 10a). The discrepancy is especially large for the scans at μ = 0.5. To some degree this may result from our reduction procedure, but mainly it is due to the lower spatial resolution of our data. However, our values are more compatible with those of Hanslmeier et al. (1990). At disc centre they measured a $\delta I_{\rm rms}/\overline{I}$ of 3.3% at λ 6495.6 Å. By considering the growth of $\delta I_{\rm rms}/\overline{I}$ with decreasing λ (cf. Fig. 11a) and with the help of the scaled Pravdjuk et al. centre-to-limb curve we estimate that the the value of $\delta I_{\rm rms}/\overline{I}$ at $\mu = 0.3$–0.4 corresponding to the Hanslmeier et al. observations is close to 2%. Consequently, we conclude that our spectra and those of Hanslmeier et al. (1990) are of similar quality.

Theoretical values of $\delta I_{\rm rms}/\overline{I}$ depend very strongly on the smoothing procedure employed to mimic seeing. As an example of this dependence we studied $\delta I_{\rm rms}/\overline{I}$ smoothed by Gaussians with dispersions of 544 km and 725 km. Although the broader function reproduces the observed value at $\mu = 0.42$ well, it produces a too strong decrease of $\delta I_{\rm rms}/\overline{I}$ with μ. After smoothing by the point spread function PSF1 proposed by Nordlund (1984a) we obtain better agreement with the CLV of the balloon observations of Pravdjuk et al. (1974) as can be seen from Fig. 10a. The model $\delta I_{\rm rms}/\overline{I}$ are, however, still too large compared to our observations. We therefore modified Nordlund's PSF1 slightly such that it describes the $\delta I_{\rm rms}/\overline{I}$ we observe near the limb. The parameters of this new PSF2 are given in Sect. 4. According to Fig. 10a the theoretical $\delta I_{\rm rms}/\overline{I}$ smeared with PSF2 agrees well with our observational data. Moreover, at the centre of the disc (Fig. 11a) the resulting theoretical $\delta I_{\rm rms}/\overline{I}$ also lies close to the value observed by Hanslmeier et al. (1990). This provides additional confirmation that our observations and those of Hanslmeier et al. (1990) are of similar quality.

5.4. Intensity fluctuations in the line cores

As reported by Hanslmeier et al. (1990) lines formed higher exhibit larger relative intensity fluctuations in their cores ($\delta r_{\rm rms}/\overline{r}$). Line observations can serve as a test of the reality of temperature fluctuations in the upper layers of our model atmospheres. The comparison of observed and theoretical $\delta r_{\rm rms}/\overline{r}$ and $\delta r_{\rm rms}$ are given in Figs. 10b, 11b and 11c.

Theoretical $\delta r_{\rm rms}/\overline{r}$ of the Ni I 4912 Å line are compared with our observations in Fig. 10b. The model results are again

presented after smearing by PSF1 (solid circles) or PSF2 (open circles). Note that the PSF2-broadened synthetic scans of the line core exhibit as good an agreement with the observations as the continuum (Fig. 10a).

$\delta r_{\rm rms}/\overline{r}$ values computed at disc centre for the lines listed in Table 1 are plotted in Figs. 11b and c. The theoretical values were computed after smoothing the simulated scans using PSF1 or PSF2. As seen from Figs. 11b and c the relative and absolute fluctuations of residual intensity in the line cores predicted by the present models agree well with the observations of Hanslmeier et al. (1990) if we smear using PSF2.

The height dependence of line intensity fluctuations has an "elbow" at a height of 400–425 km. We interpret this to be due to the reversal of the sign of temperature fluctuations (see Fig. 6). Its presence explains a decrease of intensity variations of those lines the cores of which are formed higher. These model predictions should be tested using observations of many lines formed at a range of heights, such as the set of lines we have used (Table 1).

5.5. Height dependence of theoretical correlations

Before studying the centre-to-limb variation of the observed correlations let us discuss the height dependence of the theoretical correlation coefficients, which was determined at disc centre using the lines listed in Table 1. The coefficients for the different lines are shown in Fig. 12, together with the values observed by Hanslmeier et al. (1990) for the Fe I lines at 6494.50, 6495.74, 6496.47, and 6494.99 Å.[2] In Fig. 12 we illustrate the results obtained (1) without spatial smearing and (2) using PSF2.

In Fig. 12 we have attempted to plot each correlation coefficient at the height at which it is formed (in a rough sense). Hence, correlation coefficients between quantities derived from the line core (e.g. core wavelength shift and intensity variations) are plotted vs. the height of formation of the line core (H_d), while correlation coefficients involving quantities depending on the whole line profile (i.e. half-width and equivalent width) are plotted vs. the equivalent width formation height (H_W). Finally, correlation coefficients between core and full-profile quantities are plotted vs. the average of these two heights. Although the reaction of a spectral line to fluctuations of atmospheric parameters may well depend on other properties than its height of formation, we find that the correlation coefficients scatter little around the mean curves, indicating that the dominant influence is due to the formation height.

A comparison between smeared and unsmeared correlation coefficients shows that the correlation coefficients can be distinguished according to their sensitivity to spatial resolution (Fig. 12). Correlations with low or moderate sensitivity are $\langle\delta v, \delta r\rangle$, $\langle\delta I, \delta r\rangle$, $\langle\delta EW, \delta r\rangle$, $\langle\delta I, \delta v\rangle$, $\langle\delta I, \delta EW\rangle$ and $\langle\delta v, \delta EW\rangle$. On the other hand, all correlations involving line half-width variations, are strongly sensitive, suggesting that the spatial resolution impacts significantly on these correlations also in the case of observations. Quantitative comparisons involving these correlations must therefore be given lower weight.

The problem of interpreting line parameter variations and their correlations in high spatial resolution spectra has been dis-

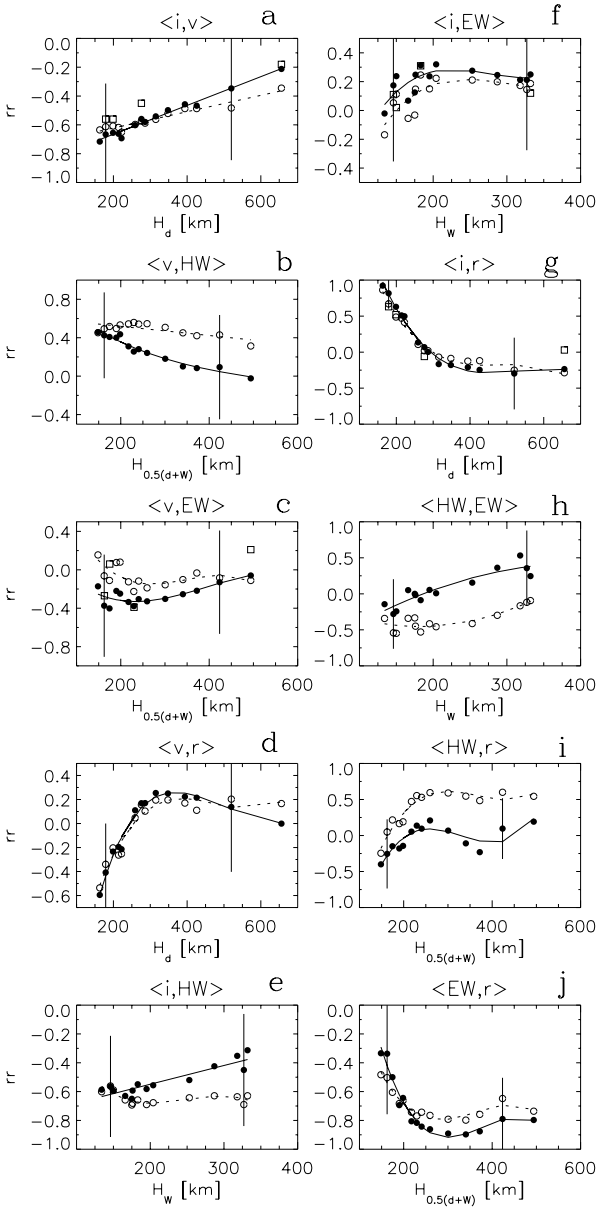

Fig. 12a–j. Synthetic correlation coefficients at disc centre for the lines listed in Table 1 as a function of their formation heights. The filled circles connected by the solid lines are the correlations obtained from the unsmeared simulations, open circles and dashed lines represent the corresponding quantities computed after smoothing by PSF2. The observational data of Hanslmeier et al. (1990) are represented by open squares. In frames **a**, **d** and **g** the correlation coefficients are plotted vs. H_d. In frames **e**, **f** and **h** they are shown as a function of H_W. In **b**, **c**, **i** and **j** the correlations are represented versus $(H_d + H_W)/2$. Error bars are estimates of standard deviations. The various plotted quantities are defined at the beginning of Sect. 5.1, respectively Sect. 5.5 in the case of H_d and H_W

[2] We do not compare our data with the evaluations of Hanslmeier et al. (1994) because those were obtained for single, selected granules and not a statistically complete sample.

cussed in several papers (e.g., Hanslmeier et al. 1994, Gadun et al. 1997). Here we only briefly note to which atmospheric quantities the various line parameters are sensitive. The variations of line half-width are mainly produced by fluctuations in gradients of the line-of-sight velocity (whereby gradients both along and across the line of sight are important). δEW is more complex. For weak and moderately strong lines it depends both on fluctuations of the vertical temperature gradient and on the horizontal distribution of the temperature in the layers which provide large contributions to line formation. For strong lines it depends significantly on the velocity field. δr largely depends on spatial variations of both the absolute value and the gradient of the temperature.

Consider now in greater detail the height dependence exhibited by the correlation coefficients resulting from the simulations (Fig. 12). All coefficients representing the correlations with δr (Figs. 12d, g, i, and j) exhibit a qualitatively similar dependence on height: a sharp change in the low photosphere and a more gradual variation in the higher layers. These correlations are also practically unaffected by spatial smearing (excluding $\langle \delta HW, \delta r \rangle$).

The strongest height dependence of all correlations is shown by $\langle \delta I, \delta r \rangle$ (Fig. 12g). For weak lines $\langle \delta I, \delta r \rangle$ is close to 1.0, mainly because r and I form at almost the same levels. For lines formed higher the models show a negative value of $\langle \delta I, \delta r \rangle$, due to the well-known reversal of horizontal temperature fluctuations above a certain height (e.g., Stein & Nordlund 1989 and Sect. 2.7 of this paper).

The correlation coefficients $\langle \delta v, \delta r \rangle$ (Fig. 12d) and $\langle \delta HW, \delta r \rangle$ (Fig. 12i) have high negative values in the layers of overshooting convection (i.e., the layers of weak-line formation) because of the largest velocities (downflows) and gradients of vertical velocities in the darkest areas.

$\langle \delta I, \delta v \rangle$ (Fig. 12a) is negative at all heights and depends monotonically on the height of line formation. Its large negative value in deep layers is typical of overshooting convection: upflows are bright, downflows are dark. However, even for the strong lines $\langle \delta I, \delta v \rangle$ remains negative. This means that to some degree the overshooting convection through the pressure affects the properties of the velocity field in the whole atmosphere under study, including layers controlled by oscillatory motions.

The coefficients $\langle \delta v, \delta EW \rangle$ (Fig. 12c) and $\langle \delta I, \delta EW \rangle$ (Fig. 12f) never differ significantly from zero, due to the many atmospheric parameters affecting δEW (as described earlier in this section; cf. Gadun et al. 1997).

The large absolute values deep in the photosphere of $\langle \delta v, \delta HW \rangle$ (Fig. 12b) and $\langle \delta I, \delta HW \rangle$ (Fig. 12e) once again reflect overshooting convection, with downflows in dark areas having the largest vertical velocity gradients (Gadun et al. 1997).

Finally, the correlation between δHW and δEW (Fig. 12h) is close to 0 for weak lines but grows to 0.5 for the stronger lines. This result is evident considering the mechanisms which control δHW and δEW. For strong lines they are similar and are connected with the variations of line-of-sight velocity over the whole range of line formation.

In Figs. 12a, c, f and g the data of Hanslmeier et al. (1990) are plotted for comparison. As we can see they are in good quantitative agreement with theoretical predictions excluding, perhaps, $\langle \delta v, \delta EW \rangle$. However, even in this case the observed and synthetic coefficients are in qualitative agreement.

The line core fluctuations are expected to be most sensitive to the change of sign of temperature fluctuations in the upper photosphere. Possibly the characteristic height dependence of $\langle \delta v, \delta r \rangle$, $\langle \delta HW, \delta r \rangle$, $\langle \delta EW, \delta r \rangle$ and to a lesser extent $\langle \delta I, \delta r \rangle$ reflects this effect and may in future be used to test the prediction of the presence of two temperature fluctuation reversals in the solar photosphere.

5.6. Centre-to-limb variation of the correlations

5.6.1. Observed correlations

The correlation coefficients derived from our observations are shown in Fig. 13 together with the correlation coefficients computed for the simulated Ni I 4912.03 Å line before and after spatial smearing by PSF2.

As follows from Fig. 13, there are only two correlation coefficients whose observed absolute values exceed 0.5 at $\mu \leq 0.5$. They are $\langle \delta HW, \delta r \rangle$ (Fig. 13i) and $\langle \delta EW, \delta r \rangle$ (Fig. 13j). Clearly, there are no significant correlations between the bulk of the parameter variations at positions close to the limb.

5.6.2. Correlations of the simulated spectra

The centre-to-limb behaviour of the synthetic correlations (Fig. 13) is a function of (1) the height dependence of physical conditions in the photosphere, e.g., the transition from overshooting convection in the low photosphere to the overlying layers, controlled by oscillations, (2) of the horizontal vs. the vertical velocity and (3) of geometrical projection effects because the two parameters involved in the correlations may be formed at different geometrical heights. Let us discuss these possibilities for some of the correlation coefficients.

With the exception of $\langle \delta I, \delta EW \rangle$, $\langle \delta HW, \delta EW \rangle$ and $\langle \delta HW, \delta r \rangle$ the absolute values of all other correlations decrease towards the solar limb.

As shown in Sect. 5.5 the correlations including δr are the most sensitive to the vertical temperature structure in the photosphere. Consequently, $\langle \delta v, \delta r \rangle$, $\langle \delta I, \delta r \rangle$ and $\langle \delta EW, \delta r \rangle$ of the weak Fe I 4911.54 Å line (not plotted), which is formed deep in the photosphere, show the opposite centre-to-limb variation relative to the moderately strong Ni I 4912.03 Å line, which is formed 40–50 km higher up according to Table 1. From Figs. 12d, g and j it follows that the weak Fe I line is formed in the layers of overshooting convection, while the effective heights at which r of the Ni I line is formed lie near its upper boundary.

Projection effects influence the correlations between the parameter variations of these lines in different ways. For the Ni I line they increase $\langle \delta I, \delta r \rangle$ because in the layers, which give the largest contribution to the Ni I line, temperature fluctuations

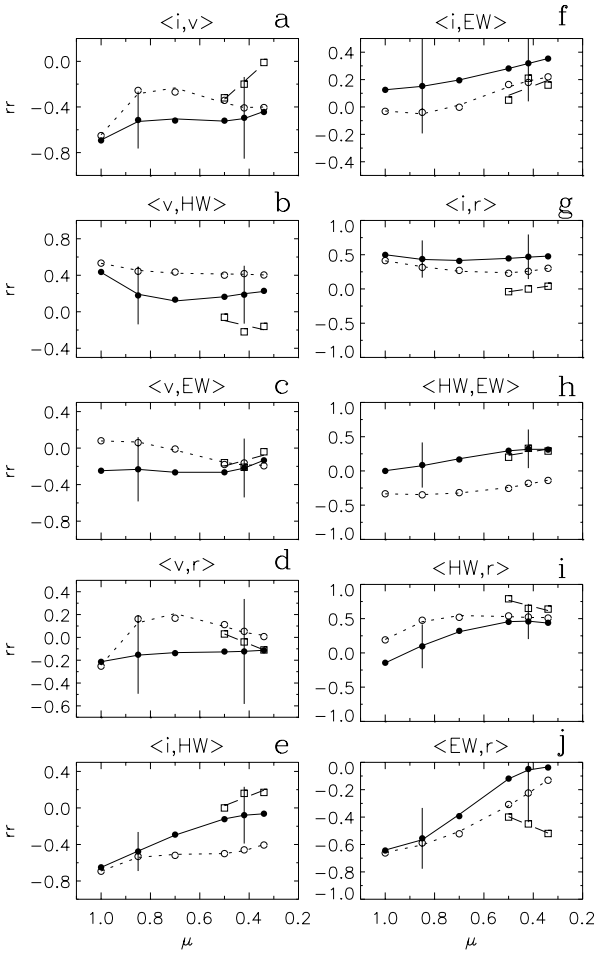

Fig. 13a–j. Variation of correlation coefficients across the solar disc. Open and filled circles are correlation coefficients obtained from simulated unsmeared and PSF2 smoothed Ni I 4912.03 Å line profiles, respectively. Open squares represent the observed values. Error bars are estimates of standard deviations

have changed sign relative to the continuum-forming layers, so that hot areas correlate with downflows. Near the limb these hot areas can be projected onto the bright granules, instead of on the dark intergranular lanes, as they are at disc centre. The formation height of the weak Fe I line, however, is sufficiently low that projection effects play no role. Correspondingly, the $\langle \delta I, \delta r \rangle$ correlation remains almost unchanged across the disc. The centre-to-limb variation of correlations other than the 3 mentioned above is qualitatively similar for both spectral lines, possibly because these correlations reflect the behaviour of the height dependence of velocity fluctuations to a much larger degree. These fluctuations do not depend on height as strongly as temperature fluctuations.

5.6.3. Comparison between observed and simulated correlations

Due to the simplifications in the modeling and as a result of the limitations and uncertainties in the observations (cf. Sects. 2 and 3) the absolute values of simulated and observed correlation coefficients may not coincide. Their centre-to-limb variations should be similar, however. Indeed, Fig. 13 confirms this expectation, with the exception of $\langle \delta I, \delta v \rangle$ and $\langle \delta EW, \delta r \rangle$. Therefore, the effects that cause the centre-to-limb variation of the synthetic correlation coefficients also appear to be present in the real solar photosphere.

Turning now to the absolute values, we note that the bulk of the observed coefficients lies near the theoretical ones computed with or without smoothing. There are, however, four correlations whose computed and observed values differ significantly. One of them is $\langle \delta I, \delta v \rangle$. The observations show a sharper loss of anticorrelation between the brightness elements and apparent Doppler velocities (Fig. 13a) near the limb. Another discrepant correlation is $\langle \delta v, \delta HW \rangle$ whose observed values are negative, in agreement with the results of Hanslmeier et al. (1994), but in contrast to the computed statistics, which predict only positive values (Fig. 13b).

The observations also reveal that near the limb the correlation between the brightness structures in the continuum and in the line core ($\langle \delta I, \delta r \rangle$ – Fig. 13g) disappears, while the 2-D models show a positive correlation. Finally, the observations exhibit a larger anticorrelation between variations of equivalent width and residual intensity in the line core ($\langle \delta EW, \delta r \rangle$ – Fig. 13j) than the simulations.

Since the use of a point spread function does not improve the correspondence with the observations one cannot explain these discrepancies as a possible influence of low spatial resolution. The discrepancy in these last 2 correlations may, however, be related to the overestimated temperature fluctuations in the middle and upper photosphere of the model, which result in higher variations of the line parameters.

On the whole the agreement between observed and simulated correlations is larger at $\mu = 1$ (Figs. 12a, c, f and g) than near the limb. This may have to do with the fact that the difference between our 2-D simulations and the 3-D Sun is more marked when seen near the limb. For example, horizontal velocities can be directed only either towards the observer or away from him in 2-D, whereas in 3-D they can also be directed perpendicularly.

Note also that the 1.5-D radiative transfer used to calculate the spectral lines leads to an overestimate of spatial variations of line parameters relative to a 2-D or 3-D approach. This was shown by Kiselman (1997, 1998) and Uitenbroek (1998) for the equivalent width of Li I 6708 Å. This may affect the correlation coefficients.

6. Discussion and conclusions

We have analysed solar granulation properties on the basis of simulated spectra emerging from 2-D hydrodynamic models. These were compared with low-spatial-resolution spectral observations made near disc centre and with high-spatial-resolution spectra obtained near the limb. In particular, we have compared line bisector shapes, wavelength shifts, continuum and line-core intensity variations, as well as the correlations be-

tween different parameters of the Ni I 4912 Å line. The comparison between the models and the high-resolution observations has once again revealed the importance of the correct point-spread-function to describe the influence of the telescope, seeing and scattered light. Not only the width of the PSF plays an important role, but also its shape. A PSF composed of the sum of two Lorentzians gives better results than a (single) Gaussian.

The present model predicts the existence of two photospheric layers at which the temperature fluctuations change sign. We point out a diagnostic of the hitherto undetected upper reversal based on high spatial resolution spectral observations of a sample of lines formed over a wide range of heights in the photosphere. Another technique that may be applied to this problem is the use of temperature-velocity phase relationships, as studied, e.g., by Deubner & Fleck (1989).

Once they are adequately smeared the models reproduce a sizable number of observations quite well, although the agreement with some other observations remains less satisfactory.

The models reproduce the centre-to-limb variation of the continuum brightness fluctuations measured with a balloon-borne telescope (Pravdjuk et al. 1974), and the correlation coefficients between a number of line and continuum parameters at disc centre. For all the lines studied the rms of core brightness fluctuations is also well reproduced. In addition, observed trends in bisectors and line shifts are well reproduced (e.g., lines with large observed bisector curvatures also have large calculated curvature, etc.), as are the actual bisector shapes of most spectral lines. Most problematic are the line shifts, with the models predicting too small blue shifts. The simulation also has some difficulty reproducing correlations between line parameters observed near the limb.

There are a number of possible reasons for the remaining shortcomings of the present models:

1. The radiative transfer, although frequency dependent, does not take NLTE effects into account, which become increasingly important in the upper atmosphere. Also, multidimensional line transfer may improve the correspondence with the observations.
2. A finer grid size may be needed to reproduce the state of the shocked gas more accurately, although tests carried out with approximately half the grid size of the present models (i.e. with 15 km) produced no significant improvement.
3. The enhanced temperature fluctuations may be related to the fact that the models are two-dimensional. Note that correlations involving the velocity (i.e. line shift) are among those showing the largest discrepancy between observations and theory. This may be pointing to a more general discrepancy in the dynamics. A detailed investigation of the velocity structure in the granulation will be the subject of a separate paper.
4. The horizontal extent of the simulations may be too small, since it is close to the maximum observed and predicted size of granules (Muller 1989, Title et al. 1989, Schüssler 1992). To test this shortcoming we have repeated a part of the present analysis using simulations spanning 17850×2030 km in the horizontal and vertical directions, respectively, with a spatial step size of 35 km. These models have been described and studied by Gadun et al. (1999a) and Ploner et al. (1998, 1999). We found that a larger horizontal size has little effect on the spatially unsmeared correlation coefficients between the various parameters, in particular also near the limb. However, the spatial smearing turned out to have a somewhat different influence on the results of the two simulations. Hence, in future larger domain sizes should be considered if the aim is to reproduce observations.

Acknowledgements. We are grateful to the referee, R. Rutten, who helped to significantly improve this paper. A. Gadun is grateful to the Swiss National Science Foundation for financial support (grant no. 7UKPJ 48440).

References

Altrock R.C., 1976, Solar Phys. 47, 517
Atroshchenko I.N., Gadun A.S., 1994, A&A 291, 635
Bellot Rubio L.R., Ruiz Cobo B., Collados M., 1999, A&A 341, L31
Belotserkovskiy O.M., Davydov Yu.M., 1982, The Method of Large Particles in Gasdynamics. Nauka, Moscow
Cattaneo F., Hurlburt N.E., Toomre J., 1989, In: Rutten R.J., Severino G. (eds.) Solar and Stellar Granulation. Kluwer, Dordrecht, p. 415
Deardorff J.W., 1971, J. Compt. Phys. 7, 120
Deardorff J.W., 1972, J. Atmos. Sci. 29, 91
Delbouille L., Neven L., Roland G., 1973, Photometric Atlas of the Solar Spectrum from λ 3000 to λ 10000. Institut d'Astrophysique, Liège
Deubner F.L., Fleck B., 1989, A&A 213, 423
Dravins D., Larsson B., Nordlund Å., 1986, A&A 158, 83
Dravins D., Lindegren L., Nordlund Å., 1981, A&A 96, 345
Dravins D., Nordlund Å., 1990a, A&A 228, 184
Dravins D., Nordlund Å., 1990b, A&A 228, 203
Espagnet O., Muller R., Roudier Th., Mein N., 1993, A&A 271, 589
Evans M.W., Harlow F.H., 1957, The Particle-in-Cell Method for Hydrodynamic Calculations. Los Alamos Sci. Lab., Los Alamos, Rept. no. LA-2139
Frutiger C., Solanki S.K., Bruls J.H.M.J., Fligge M., 1999, In: Nagendra K.N., Stenflo J.O. (eds.) Solar Polarization. Kluwer, Dordrecht, p. 281
Gadun A.S., 1986, Simulation of Turbulent Convection in the Solar Envelope. Inst. Theor. Phys., Kiev, preprint no. 96–106P
Gadun A.S., 1995, Kinemat. i Fiz. Nebesn. Tel 11, no. 3, 54
Gadun A.S., 1996, Kinemat. i Fiz. Nebesn. Tel 12, no. 4, 19
Gadun A.S., 1998, Kinemat. i Fiz. Nebesn. Tel 14, no. 3, 245
Gadun A.S., Pikalov K.N., 1996, Solar Phys. 166, 43
Gadun A.S., Sheminova V.A., 1988, SPANSAT: Program for LTE Calculations of Absorption Line Profiles in Stellar Atmospheres. Inst. Theor. Phys., Kiev, preprint No. 88–87P
Gadun A.S., Vorob'yov Yu.Yu., 1995, Solar Phys. 159, 45
Gadun A.S., Vorob'yov Yu.Yu., 1996, Astronomy Reports 40, 569
Gadun A.S., Hanslmeier A., Pikalov K.N, 1997, A&A 320, 1001
Gadun A.S., Ploner S.R.O., Hanslmeier A., et al., 1999a, A&A, in preparation (also Gadun A.S., Solanki S.K., Ploner S.R.O., et al., 1998, Size-Dependent Properties of 2-D Artificial Solar Granulation. Main Astr. Obs., Kiev, preprint no. MAO-98-4E)
Gadun A.S., Solanki S.K., Johannesson A., 1999b, In: Hanslmeier A., Messerotti M. (eds.) Motions in the Solar Atmosphere. Kluwer, Dordrecht, p. 201

Gurtovenko E.A., Sheminova V.A., Sarychev A.S., 1991, Solar Phys. 136, 239
Gustafsson B., Bell R.A., Eriksson K., Nordlund Å., 1975, A&A 42, 407
Hanslmeier A., Mattig W., Nesis A., 1990, A&A 238, 354
Hanslmeier A., Mattig W., Nesis A., 1991, A&A 251, 669
Hanslmeier A., Nesis A., Mattig W., 1994, A&A 288, 960
Hasan S.S., 1988, ApJ 332, 499
Holweger H., Müller E.A., 1974, Solar Phys. 39, 19
Keil S.L., Canfield R.C., 1978, A&A 70, 169
Kiselman D., 1997, ApJ 489, L107
Kiselman D., 1998, A&A 333, 732
Kneer F.J., Mattig W., Nesis A., Werner W., 1980, Solar Phys. 68, 31
Kurucz R.L., 1979, ApJSS 40, 1
Kurucz R.L., 1990, Atomic Spectra and Oscillator Strengths for Astrophysics and Fusion Research. North Holland, Amsterdam
Kurucz R.L., 1993, Opacities for Stellar Atmospheres: [+0.0], [+0.5],[+1.0]. CD-ROM 2
Leibacher J.W., Stein R.F., 1981, In: Jordan S. (ed.) The Sun as a Star. NASA, Washington, p. 263
Lites B.W., Nordlund Å, Scharmer G.B., 1989, In: Rutten R.J., Severino G.(eds.) Solar and Stellar Granulation. Kluwer, Dordrecht, p. 349
Malagoli A., Cattaneo F., Brummell N.H., 1990, ApJ 361, L33
Mihalas D., 1978, Stellar Atmospheres. Freeman & Co., San Francisco
Mirabel A.P., Monin R.F., 1979, Uspekhi mechanics 2, no. 3, 47
Monin A.S., Yaglom A.M., 1967, Statistical Hydromechanics. vol. 2, Nauka, Moscow, p. 439
Moore C.E., Minnaert M.G.J., Houtgast J., 1966, The Solar Spectrum 2935 Å to 8770 Å. NBS Monograph 61, Washington
Muller R., 1989, In: Rutten R.J., Severino G.(eds.) Solar and Stellar Granulation. Kluwer, Dordrecht, p. 101
Musman S., Nelson G.D., 1976, ApJ 207, 981
Nordlund Å., 1984a, In: Keil S.L. (ed.) Small-Scale Dynamical Processes in Quiet Stellar Atmospheres. SPO, Sunspot, p. 174
Nordlund Å., 1984b, In: Keil S.L. (ed.) Small-Scale Dynamical Processes in Quiet Stellar Atmospheres. SPO, Sunspot, p. 181
Nordlund Å., 1985, In: Schmidt H.U. (ed.) Theoretical Problems in High Resolution Solar Physics. MPI, München, p. 1
Nordlund Å., Dravins D., 1990, A&A 228, 155
Nordlund Å., Stein R.F., 1991, In: Crivellari L., Hubeny I., Hummer D.G. (eds.) Stellar Atmospheres: Beyond Classical Models. Kluwer, Dordrecht, p. 263
Nordlund Å., Stein R.F., 1996, In: Noels A., et al. (eds.) Stellar Evolution: What Should Be Done. Inst. d'Astrophys., Univ. Liège, Liège, p. 75
Nordlund Å., Spruit H.C., Ludwig H.-G., Trampedach R., 1997, A&A 328, 229
Orszag S.A., 1977, In: Frost W., Moulden T.H. (eds.) Handbook of Turbulence. vol. 1, Plenum Press, New York
Ploner S.R.O., Solanki S.K., Gadun A.S., Hanslmeier A., 1998, Space Sci. Rev. 85, 261
Ploner S.R.O., Solanki S.K., Gadun A.S., 1999, A&A submitted
Pravdjuk L.M., Karpinský V.N., Andreiko A.V., 1974, Solnechnye Dannye Bull. No. 2, 70
Rast M.P., Nordlund Å., Stein R.F., Toomre J., 1993, ApJ 408, L53
Roache P.J., 1972, Computational Fluid Dynamics. Albuquerque, Hermosa
Rutten R., 1988, In: Viotti R., Vittone A., Friedjung M. (eds.) Physics of Formation of Fe II Lines Outside LTE. IAU Coll. 94, Reidel, Dordrecht, p. 185
Rutten R., Kostik R.I., 1988, In: Viotti R., Vittone A., Friedjung M. (eds.) Physics of Formation of Fe II Lines Outside LTE. IAU Coll. 94, Reidel, Dordrecht, p. 83
Schüssler M., 1992, In: Schmelz J.T., Brown J.C. (eds.) The Sun — a Laboratory for Astrophysics. Kluwer, Dordrecht, p. 81
Smagorinsky J., 1963, Mon. Weather Rev. 91, 99
Solanki S.K., Steenbock W., 1988, A&A 189, 243
Solanki S.K., Rüedi I., Bianda M., Steffen M., 1996, A&A 308, 623
Spruit H.C., Nordlund Å., Title A.M., 1990, ARA&A 28, 263
Steffen M., 1989, In: Rutten R.J., Severino G.(eds.) Solar and Stellar Granulation. Kluwer, Dordrecht, p. 425
Steffen M., 1991, In: Crivellari L., Hubeny I., Hummer D.G. (eds.) Stellar Atmospheres: Beyond Classical Models. Kluwer, Dordrecht, p. 247
Steffen M., Freytag B., 1991, Rev. Mod. Astron. 4, 43
Steffen M., Muchmore D., 1988, A&A 193, 281
Stein R.F., Nordlund Å., 1989, ApJ 342, L95
Stein R.F., Nordlund Å., 1998, ApJ 499, 914
Stein R.F., Nordlund Å., Kuhn J.R., 1989, In: Rutten R.J., Severino G.(eds.) Solar and Stellar Granulation. Kluwer, Dordrecht, p. 381
Title A.M., Tarbell T.D., Topka K.P., et al., 1989, In: Rutten R.J., Severino G.(eds.) Solar and Stellar Granulation. Kluwer, Dordrecht, p. 225
Uitenbroek H, 1998, ApJ 498, 427
Unsöld A., 1955, Physik der Sternatmosphären. Springer Verlag, Berlin
Wöhl H., Nordlund Å., 1985, Sol. Phys. 97, 213